









Strain-stabilized superconductivity

J. P. Ruf ¹✉, H. Paik^{2,3}, N. J. Schreiber³, H. P. Nair³, L. Miao¹, J. K. Kawasaki ^{1,4}, J. N. Nelson ¹, B. D. Faeth^{1,2}, Y. Lee¹, B. H. Goodge ^{5,6}, B. Pamuk⁵, C. J. Fennie ⁵, L. F. Kourkoutis ^{5,6}, D. G. Schlom ^{3,6,7} & K. M. Shen ^{1,6}✉

Superconductivity is among the most fascinating and well-studied quantum states of matter. Despite over 100 years of research, a detailed understanding of how features of the normal-state electronic structure determine superconducting properties has remained elusive. For instance, the ability to deterministically enhance the superconducting transition temperature by design, rather than by serendipity, has been a long sought-after goal in condensed matter physics and materials science, but achieving this objective may require new tools, techniques and approaches. Here, we report the transmutation of a normal metal into a superconductor through the application of epitaxial strain. We demonstrate that synthesizing RuO₂ thin films on (110)-oriented TiO₂ substrates enhances the density of states near the Fermi level, which stabilizes superconductivity under strain, and suggests that a promising strategy to create new transition-metal superconductors is to apply judiciously chosen anisotropic strains that redistribute carriers within the low-energy manifold of *d* orbitals.

¹Department of Physics, Laboratory of Atomic and Solid State Physics, Cornell University, Ithaca, NY 14853, USA. ²Platform for the Accelerated Realization, Analysis, and Discovery of Interface Materials, Cornell University, Ithaca, NY 14853, USA. ³Department of Materials Science and Engineering, Cornell University, Ithaca, NY 14853, USA. ⁴Department of Materials Science and Engineering, University of Wisconsin, Madison, WI 53706, USA. ⁵School of Applied and Engineering Physics, Cornell University, Ithaca, NY 14853, USA. ⁶Kavli Institute at Cornell for Nanoscale Science, Ithaca, NY 14853, USA. ⁷Leibniz-Institut für Kristallzüchtung, Max-Born-Str. 2, Berlin 12489, Germany. ✉email: jpr239@cornell.edu; kmshen@cornell.edu

In typical weak-coupling theories of superconductivity, the effective attraction V between electrons is mediated by the exchange of bosons having a characteristic energy scale ω_B , and superconductivity condenses below a transition temperature T_c parameterized as¹:

$$T_c \sim \omega_B \exp\left(-\frac{1}{N(E_F)V}\right) = \omega_B \exp\left(-\frac{1+\lambda}{\lambda-\mu^*}\right), \quad (1)$$

where $N(E_F)$ is the density of states (DOS) near the Fermi level, λ is the electron–boson coupling strength, and μ^* is the Coulomb pseudopotential that describes the residual Coulomb repulsion between quasiparticles². For simplicity, we assume that all of the non-isotropic \mathbf{q} - and \mathbf{k} -dependencies that appear in a more realistic formulation of Cooper pairing have been averaged away. Note that within the range of validity of Eq. (1)—viz., $1 \gg \lambda > \mu^*$ —increasing λ (increasing μ^*) generally enhances (suppresses) T_c , respectively, assuming that superconductivity remains the dominant instability.

Experimental methods that boost T_c are highly desired from a practical perspective. Furthermore, by analyzing how these available knobs couple to the normal-state properties on the right side of Eq. (1), one can envisage engineering the electronic structure and electron–boson coupling to optimize T_c . For example, increasing $N(E_F)$ is a frequently suggested route towards realizing higher T_c , but how to achieve this for specific materials often remains unclear.

Historically, chemical doping and hydrostatic pressure have been the most common knobs used to manipulate superconductivity. Unfortunately, doping has the complication of explicitly introducing substitutional disorder, whereas pressure studies are incompatible with most probes of electronic structure. Moreover, because large pressures are usually required to appreciably increase T_c ³, pressure-enhanced superconductivity exists transiently—oftentimes in different structural polymorphs than at ambient conditions—rendering it inaccessible for applications.

An alternative strategy for controlling superconductivity is epitaxial strain engineering. This approach is static, disorder-free, allows for the use of sophisticated experimental probes⁴, and enables integration with other materials in novel artificial interfaces and device structures^{5,6}. To date, epitaxial strain has only been used to modulate T_c in known superconductors^{7–12}. In this article, we describe the creation of a new superconductor through epitaxial strain, starting from a compound, RuO₂, previously not known to be superconducting. By comparing the results of angle-resolved photoemission spectroscopy (ARPES) experiments with density functional theory (DFT) calculations, we show that splittings between the effective low-energy d orbital degrees of freedom in RuO₂ respond sensitively to appropriate modes of strain, and we discuss how this approach may open the door to strain tuning of superconductivity in other materials.

Results

Electrical and structural characterization of RuO₂ thin films.

Bulk RuO₂ crystallizes in the ideal tetragonal rutile structure (space group #136, $P4_2/mnm$) with lattice constants at 295 K of ($a = 4.492 \text{ \AA}$, $c = 3.106 \text{ \AA}$)¹³. RuO₂ thin films in distinct epitaxial strain states were synthesized using oxide molecular-beam epitaxy (MBE) by employing different orientations of isostructural TiO₂ substrates, ($a = 4.594 \text{ \AA}$, $c = 2.959 \text{ \AA}$)¹⁴. As shown in Fig. 1a, b, the surfaces of (101)-oriented substrates are spanned by the $[\bar{1}01]$ and $[010]$ lattice vectors of TiO₂, which ideally impart in-plane tensile strains on RuO₂ (at 295 K) of +0.04% and +2.3%, respectively. On TiO₂(110), the lattice mismatches with RuO₂ are larger: −4.7% along $[001]$ and +2.3% along $[\bar{1}10]$.

Figure 1c shows electrical resistivity $\rho(T)$ measurements for RuO₂ films, along with results for bulk RuO₂ single crystals from Ref. 15. To compare with bulk, for the thin-film samples we plot the geometric mean of the components of ρ along the two in-plane directions; the intrinsic resistive anisotropy is known to be small¹⁶, consistent with our findings (Supplementary Note 1 and Supplementary Fig. 1). $\rho(T)$ data for the lightly strained RuO₂/TiO₂(101) sample—henceforth referred to as RuO₂(101)—are nearly indistinguishable from bulk, exhibiting metallic behavior with a low residual resistivity $\rho(0.4 \text{ K}) < 2 \text{ } \mu\Omega\text{-cm}$. In contrast, a clear superconducting transition is observed for the more heavily strained RuO₂/TiO₂(110) sample—referred to as RuO₂(110)—at $T_c = 2.0 \pm 0.1 \text{ K}$.

Magnetoresistance measurements (Fig. 1e, f) with H_{\perp} applied along $[110]$ (the out-of-plane direction) show a monotonic suppression of T_c with increasing fields and an extrapolated value of $H_{cL}(T \rightarrow 0 \text{ K}) = 13.3 \pm 1.5 \text{ kOe}$, corresponding to an average in-plane superconducting coherence length of $\xi(T \rightarrow 0 \text{ K}) = 15.8 \pm 0.9 \text{ nm}$ (Supplementary Note 2 and Supplementary Fig. 2). In Fig. 1d, we show a $V(I)$ curve measured on a lithographically patterned resistivity bridge at $T/T_c = 0.3$, from which we extract a critical current density $J_c = (9.5 \pm 1.2) \times 10^4 \text{ A/cm}^2$. This large value of J_c (over one order of magnitude larger than values reported on typical elemental superconductors with comparable T_c s) indicates that the superconductivity in RuO₂(110) does not arise from a filamentary network, structural defects, minority phases, or from the substrate–film interface, which would all yield much smaller values of J_c .

In order to disentangle the effects of strain from other possible sources of superconductivity, we compare RuO₂ films as functions of strain and film thickness, t . In Fig. 2a, we plot x-ray diffraction (XRD) data from similar-thickness films of RuO₂(101) and RuO₂(110), showing that the bulk-averaged crystal structures of the films are strained as expected along the out-of-plane direction based on their net in-plane lattice mismatches with TiO₂. The primary 101 and 202 film peaks of RuO₂(101) are shifted to larger angles than bulk RuO₂, corresponding to a 1.1% compression of d_{101} , while Nelson–Riley analysis of the primary 110, 220, and 330 (see, e.g., Supplementary Fig. 4) peak positions for RuO₂(110) evidence a 2.0% expansion of d_{110} relative to bulk. In Fig. 2b, c, we plot resistivity data showing that reducing t in RuO₂(110) decreases T_c , as is commonly observed in numerous families of thin-film superconductors^{17,18}, with T_c dropping below our experimental threshold (0.4 K) between $t = 11.5$ and 5.8 nm. This suppression of T_c with thickness indicates superconductivity is not confined near the substrate–film interface, so possible interfacial modifications of the crystal structure¹⁹, carrier density²⁰, substrate–film mode coupling²¹, and non-stoichiometry in the films or substrates^{22–24} can all be eliminated as potential causes of superconductivity. These conclusions are also supported by the facts that superconductivity is not observed in RuO₂(101) films, nor in bare TiO₂ substrates treated in an identical fashion to the RuO₂ films. Finally, in Fig. 2d we include a scanning transmission electron microscopy (STEM) image of a superconducting RuO₂(110) sample, which confirms uniform growth of the film over lateral length scales exceeding those expected to be relevant for superconductivity (e.g., ξ), and shows a chemically abrupt interface between RuO₂ and TiO₂ (Supplementary Fig. 5), with no evidence of minority phases.

We believe the thickness dependence of T_c results primarily from the competition between: (i) an intrinsic strain-induced enhancement of T_c that should be maximized for thinner, commensurately strained RuO₂(110) films, versus (ii) disorder-induced suppressions of T_c that become amplified in the ultrathin limit (see, e.g., ρ_0 versus t in Fig. 2c). While the thinnest films

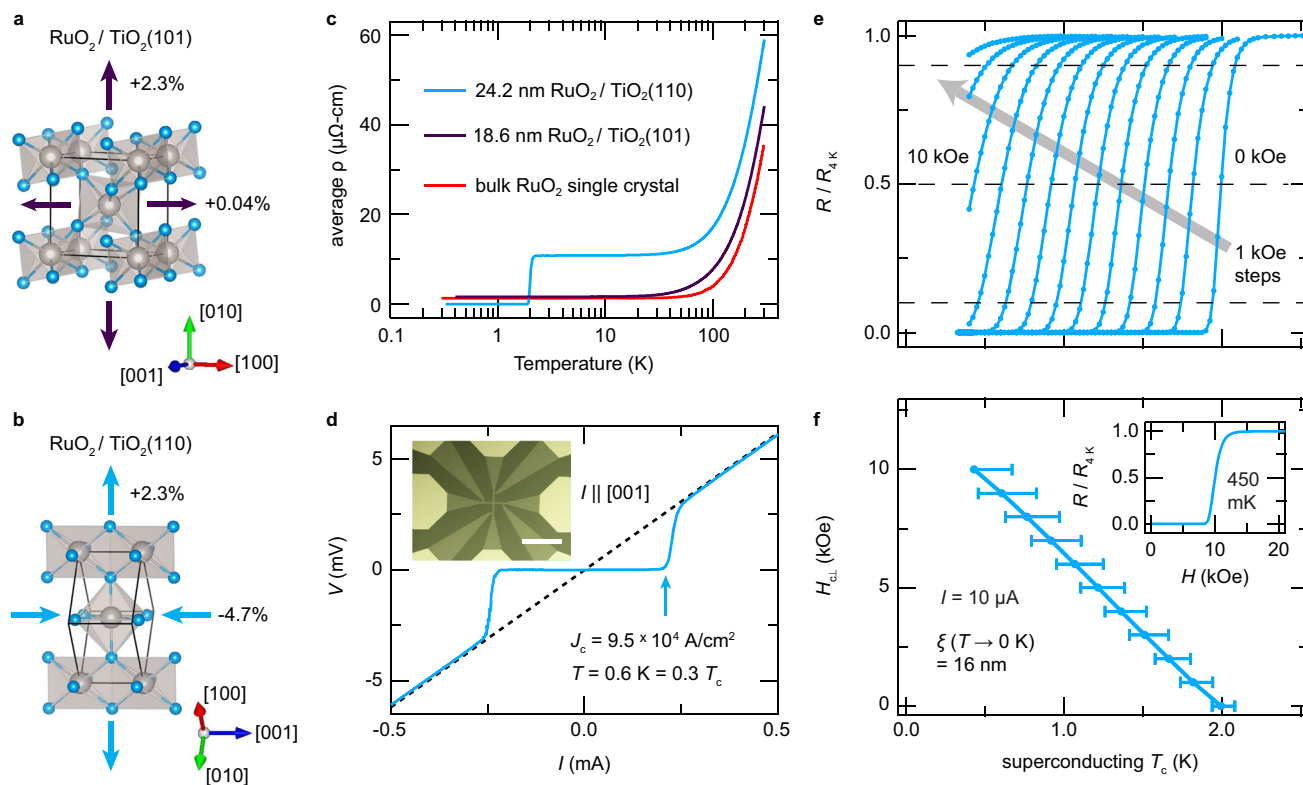


Fig. 1 Electrical transport behavior of bulk RuO_2 single crystals and epitaxially strained RuO_2 thin films. **a, b** Schematic diagrams of the crystal structures and in-plane lattice mismatches with TiO_2 substrates of RuO_2 thin films synthesized in (101)- and (110)-orientations. Gray and blue spheres represent Ru and O atoms, respectively. **c** Average resistivity versus temperature curves for 24.2 nm thick $\text{RuO}_2(110)$ and 18.6 nm thick $\text{RuO}_2(101)$ films, compared to results for bulk RuO_2 single crystals from Ref. ¹⁵. For clarity the bulk RuO_2 data have been rigidly shifted upward by $1 \mu\Omega\text{-cm}$ ($\rho_0 \approx 0.3 \mu\Omega\text{-cm}$). **d** $V(I)$ curve measured at 0.6 K on a $10 \mu\text{m}$ -wide resistivity bridge lithographically patterned on the $\text{RuO}_2(110)$ sample from (c) (as shown in the inset: scale bar = $200 \mu\text{m}$), which has the direction of current flow parallel to $[001]_{\text{rutile}}$. Similarly large critical current densities J_c are obtained with $I \parallel [1\bar{1}0]$ (Supplementary Note 1 and Supplementary Fig. 1). **e, f** Upper critical magnetic fields $H_{c\perp}$ versus superconducting T_c s extracted from magnetoresistance measurements for the $\text{RuO}_2(110)$ sample in (c) along with a characteristic $R(H)$ sweep acquired at 0.45 K (inset in (f)). Superconducting T_c s are taken as the temperatures at which the resistance crosses 50% of its residual normal-state value $R_{4\text{K}}$; error bars on these T_c s indicate where R crosses the 90% and 10% thresholds of $R_{4\text{K}}$, respectively (cf. the horizontal dashed lines in (e)).

experience the largest substrate-imposed strains, stronger disorder scattering (likely from interfacial defects) reduces T_c below our detection threshold. Films of intermediate thickness ($t \approx 10\text{--}30 \text{ nm}$) have lower residual resistivities and higher T_c s, but do exhibit signatures of partial strain relaxation. Nevertheless, a detailed analysis of misfit dislocations by STEM and XRD reciprocal-space mapping (Supplementary Notes 3, 4 and Supplementary Figs. 8–10) indicates that these films are largely structurally homogeneous and, on average, much closer to commensurately strained than fully relaxed. Finally, in much thicker samples (e.g., $t = 48 \text{ nm}$) where a more significant volume fraction of the film should be relaxed, the strain is further released by oriented micro-cracks that make such samples spatially inhomogeneous and cause severely anisotropic distributions of current flow, preventing reliable resistivity measurements (Supplementary Fig. 11).

DFT calculations and ARPES measurements. Having established the strain-induced nature of the superconductivity in $\text{RuO}_2(110)$, we now explore its underlying origin using a combination of DFT and ARPES. In Fig. 3a, we present the electronic structure of commensurately strained $\text{RuO}_2(110)$ calculated by DFT + U ($U = 2 \text{ eV}$), following the methods of Berlijn et al.¹³. Despite being constructed of RuO_6 octahedra having the same $4d^4$ electronic configuration as in $(\text{Ca,Sr,Ba})\text{RuO}_3$, the electronic structure of RuO_2 is markedly different from that of perovskite-

based ruthenates. These distinctions arise from a sizable ligand-field splitting of the t_{2g} orbitals, such that the most natural description of the low-energy electronic structure is in terms of states derived from two distinct types of orbitals: $d_{||}$ and (d_{xz}, d_{yz}) , as illustrated by plots of Wannier functions in Fig. 3b^{25,26}. Viewed in the band basis in Fig. 3a, the differentiation in \mathbf{k} -space between these orbitals becomes apparent: the near- E_F $d_{||}$ states (yellow-orange) form mostly flat bands concentrated around the $k_{001} = \pi/c$ (i.e., Z-R-A) plane, whereas the (d_{xz}, d_{yz}) states (purple) form more isotropically dispersing bands distributed uniformly throughout the Brillouin zone.

In many other d^4 ruthenates (such as Sr_2RuO_4 and Ca_2RuO_4), static mean-field electronic structure calculations (such as DFT + U) often predict quantitatively incorrect effective masses^{27–31}—and sometimes even qualitatively incorrect ground states³²—because these approaches neglect local (atomic-like) dynamical spin-orbital correlations (driven by Hund’s rules) that strongly renormalize the low-energy quasiparticle excitations. Therefore, it is imperative to compare DFT calculations for RuO_2 with experimental data, to establish the reliability of any theoretically predicted dependence of the electronic structure on strain. The left half of Fig. 3d shows the Fermi surface of $\text{RuO}_2(110)$ measured with He- 1α (21.2 eV) photons at 17 K, which agrees well with a non-magnetic DFT + U simulation of the Fermi surface at a reduced out-of-plane momentum of $k_{110} = -0.2 \pm 0.2 \pi/d_{110}$ (right half of Fig. 3d). In Fig. 3e, f, we

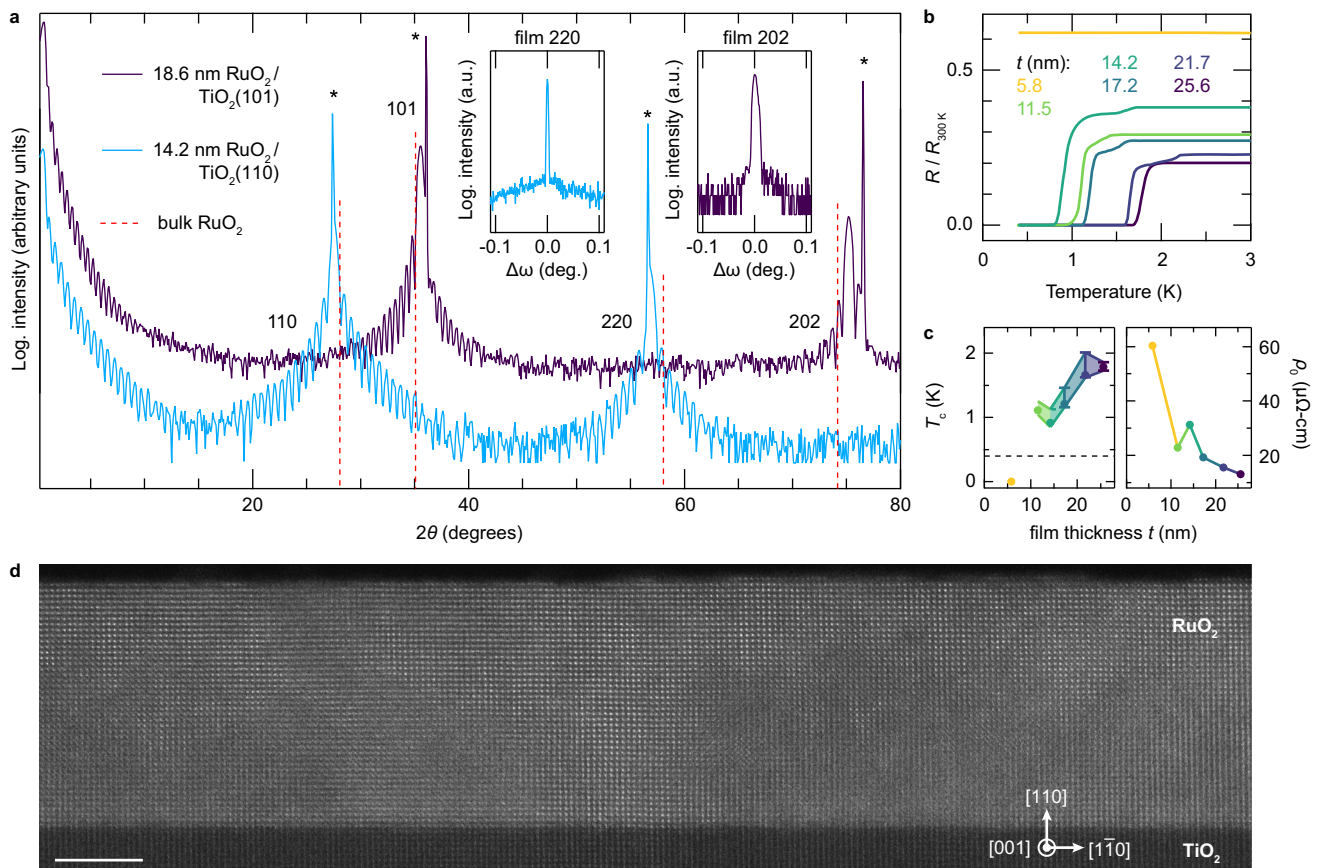


Fig. 2 Structural characterization of epitaxially strained RuO₂ thin films, and film-thickness-dependent superconductivity for RuO₂(110). **a** XRD data acquired with Cu-K α radiation along the specular crystal truncation rods for 18.6 nm thick RuO₂(101) and 14.2 nm thick RuO₂(110) films. Bragg peaks arising from the TiO₂ substrates are marked with asterisks, and the peak positions that would be expected for unstrained bulk RuO₂ are indicated by dashed red lines¹³. Insets display rocking curves with FWHMs < 0.01° acquired at the 2θ values corresponding to the primary 220 and 202 film peaks. Here q_{\parallel} is aligned with TiO₂[$\bar{1}\bar{1}0$] for the (110)-oriented sample, and with TiO₂[$\bar{1}0\bar{1}$] for the (101)-oriented sample. **b** Resistance versus temperature curves for RuO₂(110) samples with different film thicknesses t , normalized to their values at 300 K. **c** Superconducting T_c s and residual resistivities ρ_0 plotted versus film thickness for the RuO₂(110) samples from (b). Error bars on T_c s have the same meaning as in Fig. 1. The horizontal dashed line represents the base temperature attainable in our refrigerator, 0.4 K. **d** STEM image of the same 14.2 nm thick RuO₂(110) sample from (a–c) (scale bar = 5 nm). More comprehensive structural and electrical characterization of the samples shown here are included in Supplementary Notes 3, 4 and Supplementary Figs. 3–10.

plot energy versus momentum spectra acquired along the white dashed lines in Fig. 3d: in Fig. 3e, the spectrum is dominated by the flat d_{\parallel} bands centered around a binding energy of 300 meV, whereas in Fig. 3f the (d_{xz}, d_{yz}) -derived bands are steeply dispersing and can be tracked down to several hundred meV below E_F , both of which are well reproduced by DFT + U calculations. The reasonable agreement between the experimentally measured and DFT band velocities is consistent with recent ARPES studies of Ir-doped RuO₂ single crystals³³ and with earlier specific heat measurements of the Sommerfeld coefficient in bulk RuO₂, which suggested a modest momentum-averaged quasiparticle mass renormalization of $\gamma_{\text{exp.}} = 1.45\gamma_{\text{DFT}}$ ^{34,35}. The fact that the true electronic structure of RuO₂ can be well accounted for by DFT + U allows us to utilize such calculations to understand how epitaxial strains can be employed to engineer features of the electronic structure to enhance the instability towards superconductivity.

Evolution of electronic structure under strain. In Fig. 4a, we show the strain dependence of the DFT-computed band structure and DOS for RuO₂(110), RuO₂(101), and bulk RuO₂. While the results for RuO₂(101) are almost identical to bulk, the results for RuO₂(110) exhibit significant differences: the large d_{\parallel} -derived peak in the DOS (centered around a binding energy of 800 meV

for bulk) is split into multiple peaks for RuO₂(110), several of which are shifted closer to the Fermi level, thereby increasing $N(E_F)$. In our studies, we found that this strain-dependent trend was robust against details of the DFT calculations, such as whether U was finite (Supplementary Note 5 and Supplementary Fig. 12). In order to determine whether this strain dependence of $N(E_F)$ is realized in experiment, we compared the electronic structure of a thin (7 nm) highly strained RuO₂(110) film with a much thicker (48 nm) partially strain-relaxed RuO₂(110) film. The surface lattice constants of the 48 nm thick film were closer to bulk RuO₂ than the 7 nm thick film (Supplementary Note 7 and Supplementary Fig. 14), so we expect that the surface electronic structure probed by ARPES of the thicker film to be more representative of bulk RuO₂. Comparisons between the RuO₂(110) and RuO₂(101) surfaces are less straightforward, since different parts of the three-dimensional Brillouin zone are sampled by ARPES (Supplementary Note 8 and Supplementary Fig. 15). Figure 4b shows $E(k)$ spectra side by side for the 7 nm (left) and 48 nm (right) films of RuO₂(110) along the same cut through k -space from Fig. 3e where the photoemission intensity is dominated by d_{\parallel} initial states. The higher levels of strain present at the film surface for the 7 nm thick sample cause a substantial shift of the flat bands towards E_F by 120 ± 20 meV relative to the more strain-relaxed 48 nm thick sample. Integrating the

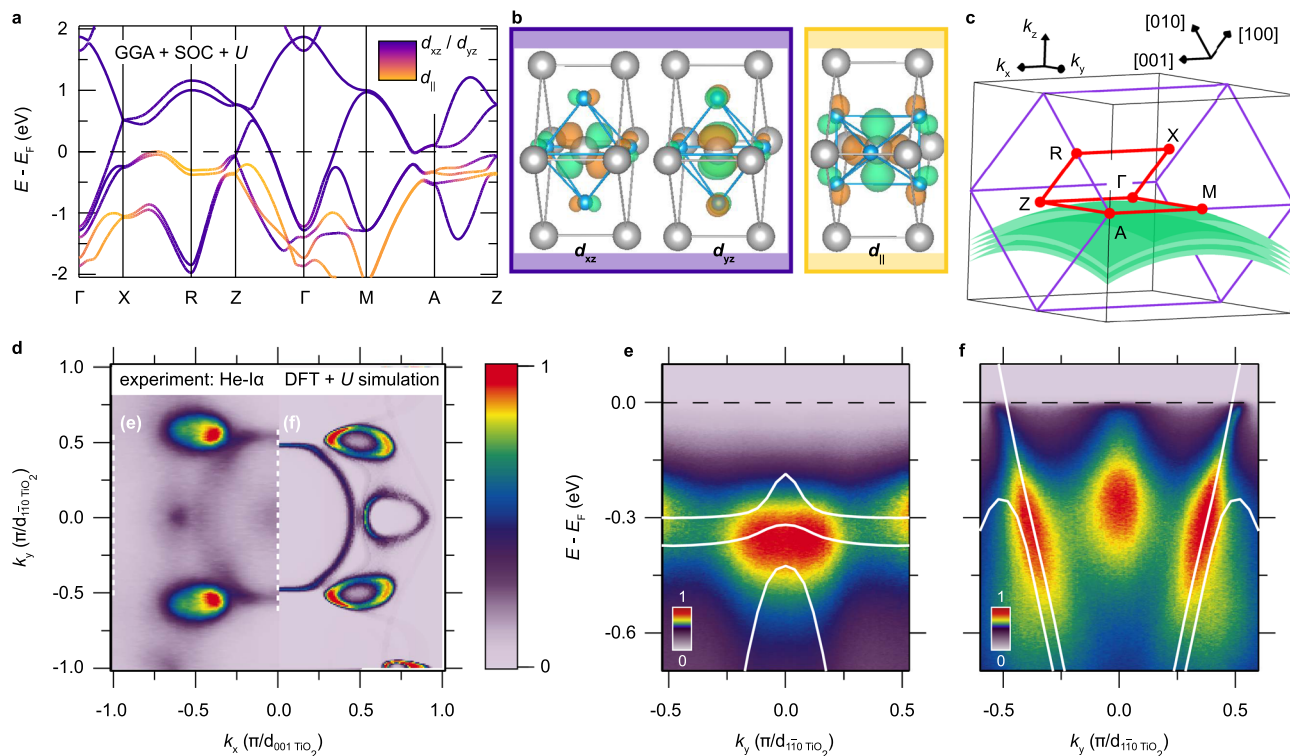


Fig. 3 Electronic structure of RuO₂. **a** Non-magnetic band structure of RuO₂(110) according to DFT, calculated within the generalized gradient approximation (GGA) including spin-orbit coupling (SOC) and a static $+U = 2$ eV correction on the Ru sites. The color scale indicates the magnitudes of projections of the Kohn-Sham eigenstates at each \mathbf{k} onto Ru-centered Wannier functions with d_{\parallel} and (d_{xz}, d_{yz}) orbital characters, which are constructed from the manifold of self-consistent eigenstates spanning E_F and are plotted in drawings of the crystal structure in **(b)**. Ru (O) atoms are colored gray (blue), as in Fig. 1a, b. Green and orange surfaces in **(b)** represent isosurfaces of the Wannier functions that have equal absolute magnitudes, but opposite (i.e., positive and negative) signs, respectively. **c** Brillouin zone schematic defining the coordinate system utilized for describing ARPES measurements of the electronic structure on (110)-oriented surfaces: $k_x \parallel [001]_{\text{rutile}}$, $k_y \parallel [\bar{1}\bar{1}0]_{\text{rutile}}$, and $k_z \parallel [110]_{\text{rutile}}$. The Brillouin zone of the parent tetragonal rutile structure is outlined in purple, the high-symmetry contour for the spaghetti plot from **(a)** is colored red, and the region probed on (110)-oriented surfaces with He-I α photons (21.2 eV) is shaded green (Supplementary Note 6 and Supplementary Fig. 13). **d** Slice through the Fermi surface experimentally measured for a 7 nm thick RuO₂(110) film (left), compared to the Fermi surface from DFT + U simulations (right) projected onto the region of the Brillouin zone colored green in **(c)**. $E(k)$ spectra acquired along the one-dimensional cuts indicated by dashed white lines in **(d)** show: **e** flat bands with d_{\parallel} orbital character and **f** more dispersive bands with (d_{xz}, d_{yz}) character, both consistent with DFT + U expectations (solid white lines). The intensities of the experimental data shown in **(d-f)** and of the DFT simulations shown in **(d)** are plotted in arbitrary units where we define 0 (1) to be the minimum (maximum) value, respectively, of the given data set. Only relative changes in intensity within a given panel (as visualized by the false color scales) are meaningful.

ARPES data over the full measured region of \mathbf{k} -space for both samples gives the average energy distribution curves plotted in Fig. 4c, which show that spectral weight near E_F is enhanced as the d_{\parallel} states move towards E_F , in qualitative agreement with the trend predicted by DFT. Our results indicate that the primary electronic effect of the epitaxial strains in RuO₂(110) is to alter the relative occupancies of the d_{\parallel} and (d_{xz}, d_{yz}) orbitals as compared with bulk, and to push a large number of states with d_{\parallel} character closer to E_F , which enhances $N(E_F)$ and likely T_c .

Discussion

Observations of Fermi-liquid-like quasiparticles near E_F ^{34,36–38} that scatter at higher energies primarily via their interaction with phonons^{16,35}, along with the fact that superconductivity in RuO₂(110) persists in the dirty limit (Supplementary Note 4 and Supplementary Fig. 9), are both consistent with conventional Cooper pairing, suggesting that calculations assuming an electron-phonon mechanism may be enlightening. We performed DFT-based Migdal-Eliashberg calculations of T_c for bulk RuO₂ and commensurately strained RuO₂(110) that indeed indicate epitaxial strain can enhance T_c by several orders of magnitude. For bulk RuO₂, we find that the empirical Coulomb

pseudopotential must satisfy $\mu^* > 0.30$ to be compatible with the experimentally measured least upper bound on T_c ($T_c < 0.3$ K¹⁵). For this range of μ^* , T_c for RuO₂(110) can be as high as 7 K (Supplementary Note 9 and Supplementary Fig. 16). A robust strain-induced enhancement of the electron-phonon coupling $\lambda_{\text{el-ph}}$ boosts T_c by a factor of 20 (for $\mu^* = 0.30$), and this ratio becomes even larger for higher values of μ^* —e.g., for $\mu^* = 0.37$, $T_c(110)/T_c(\text{bulk}) = 5$ K/5 mK). Although these estimations of T_c are broadly consistent with our experimental findings, conventional superconductivity in RuO₂ remains a working hypothesis until measurements of the order parameter are possible.

In principle, assuming that all Fermi liquids are eventually unstable towards some channel(s) of Cooper pairing at sufficiently low temperatures and magnetic fields (including internal fields arising from magnetic impurities), the strain-stabilized superconductivity observed here in RuO₂ is not strictly a change in the ground state of the system. For our purposes, however, extremely low temperatures and fields below what are experimentally achievable can be regarded as effectively zero, justifying our use of phrases such as strain-induced superconductivity interchangeably with huge enhancement of critical temperature. If we limit the scope of this semantic discussion to conventional,

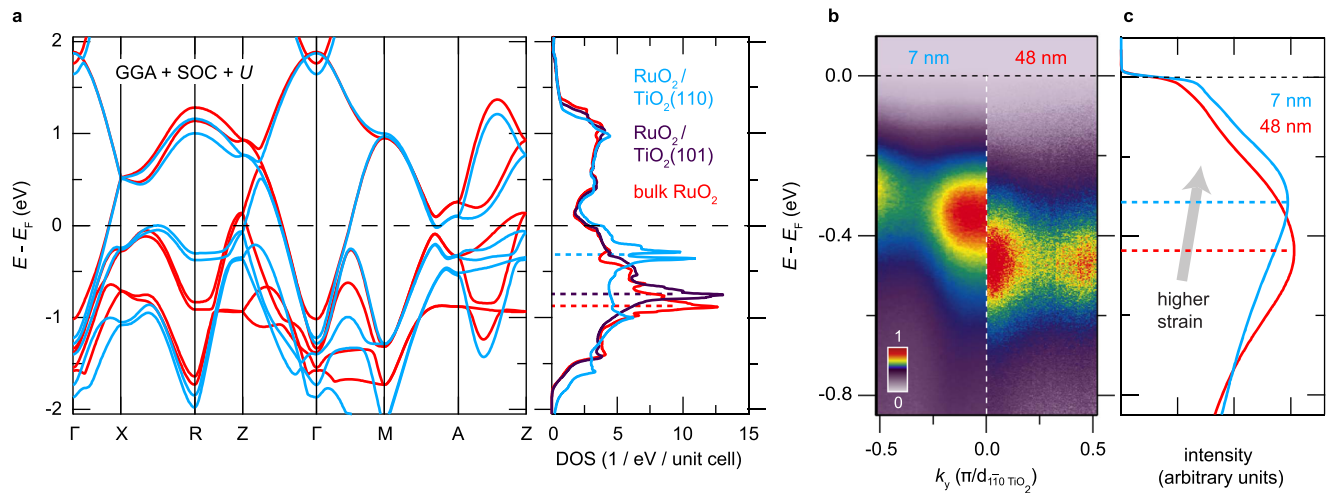


Fig. 4 Strain-induced changes to the electronic structure of RuO₂. **a** DFT + *U* (*U* = 2 eV) band structures and corresponding density of states (DOS) traces for bulk RuO₂ and epitaxially strained RuO₂(110) and RuO₂(101) thin films. The RuO₂(101) results are omitted from the spaghetti plot for clarity since they are very similar to bulk. **b** Comparison of *E*(*k*) spectra along the cut shown in Fig. 3e for two different RuO₂(110) samples: a highly strained 7 nm thick film (left), and a partially strain-relaxed 48 nm thick film (right). The false color scale used to visualize the intensities in each spectrum is defined and normalized in the same way as in Fig. 3. **c** As an approximate proxy of the total DOS, for these samples we plot the energy distribution curves of photoemission intensity averaged over the entire region of *k*-space probed experimentally with 21.2 eV photons (cf. Fig. 3c), which demonstrate that the epitaxial strains imposed by TiO₂(110) substrates shift *d*_{||} states towards *E*_{*F*} and thereby increase *N*(*E*_{*F*}).

non-sign-changing (*s*-wave) order parameters, we note that in the presence of Coulomb repulsion and other effects, an instability towards *s*-wave superconductivity is not present in every system; the electron–phonon coupling generally must exceed some finite critical value. In the present context, the effects of strain reported in this article might be boosting the electron–phonon coupling above the critical value appropriate for RuO₂, thus inducing a new *s*-wave state that is absent (even in theory) for the unstrained material.

We believe our results demonstrate that a promising strategy to create new transition-metal superconductors is to apply judiciously chosen anisotropic strains that modulate degeneracies among *d* orbitals near *E*_{*F*}. Many classic studies of conventional superconductors that have nearly-free-electron states spanning *E*_{*F*} derived from (*s*, *p*) orbitals actually show decreases in *T*_{*c*} under hydrostatic pressure³⁹, due to lattice stiffening dominating over any pressure-induced changes to the Hopfield parameter⁴⁰. In a limited number of elemental metals where *T*_{*c*} monotonically increases under pressure (such as vanadium⁴¹), pressure-induced electron transfer between *s* → *d* orbitals has been suggested as a likely cause of the enhanced transition temperatures³; a drawback of this approach, however, is that large pressures of ≈ 10 GPa are typically required to, e.g., double *T*_{*c*}. More recently, measurements on single crystals of the unconventional superconductor Sr₂RuO₄ have shown that appropriately oriented uniaxial pressures of only ≈ 1 GPa can boost *T*_{*c*} by more than a factor of two⁴². Independent of the underlying mechanism, it appears that anisotropic strains may prove to be significantly more efficacious than hydrostatic pressure for tuning superconductivity in multi-orbital systems, as shown here for RuO₂, as well as in Sr₂RuO₄.

Sizable coupling between the lattice and electronic degrees of freedom in rutile-like crystal structures has been well established both theoretically²⁶ and experimentally in VO₂, where strain-induced variations in the orbital occupancies can be used to modify the metal-insulator transition temperature by $\delta T_{\text{MIT}} \approx 70$ K^{43,44}. Therefore, it may be promising to explore other less strongly correlated (i.e., 4*d* and 5*d*) rutile compounds such as MoO₂ for strain-stabilized superconductivity, instead of employing chemical doping^{45–47}. Finally, since RuO₂/TiO₂(110)

is the first known stoichiometric superconductor within the rutile family, further optimization of the superconductivity may enable the creation of structures that integrate superconductivity with other functional properties that have been extensively studied in other rutile compounds, such as high photocatalytic efficiency, half-metallic ferromagnetism, and large spin Hall conductivities.

Methods

Film synthesis. Epitaxial thin films of RuO₂ were synthesized on various orientations of rutile TiO₂ substrates using a GEN10 reactive oxide MBE system (Veeco Instruments). Prior to growth, TiO₂ substrates (Crystec, GmbH) were cleaned with organic solvents, etched in acid, and annealed in air to produce starting surfaces with step-terrace morphology, following the methods in Ref. 48. Elemental ruthenium (99.99% purity, ESPI Metals) was evaporated using an electron-beam evaporator in background oxidant partial pressures of $1 \times 10^{-6} - 5 \times 10^{-6}$ Torr of distilled ozone (≈ 80% O₃ + 20% O₂) at substrate temperatures of 250–400 °C, as measured by a thermocouple. Reflection high-energy electron diffraction was used to monitor the surface crystallinity of the films in situ and showed characteristic oscillations in intensity during most of the Ru deposition, indicating a layer-by-layer growth mode following the initial nucleation of several-monolayer-thick RuO₂ islands⁴⁹.

Film characterization. The crystal structures of all RuO₂ thin-film samples were characterized via lab-based x-ray diffraction (XRD) measurements with Cu-*K* α radiation (Rigaku SmartLab and Malvern Panalytical Empyrean diffractometers). Four-point-probe electrical transport measurements were conducted from 300 K down to a base temperature of 0.4 K using a Physical Properties Measurement System equipped with a He-3 refrigerator (Quantum Design). All RuO₂/TiO₂(110) samples were superconducting with *T*_{*c*}s ranging from 0.5 to 2.4 K, except for ultrathin films with residual resistivities $\rho_0 \approx 40$ $\mu\Omega$ -cm, as shown in Fig. 2 and Supplementary Fig. 9.

A subset of films studied by XRD and transport were also characterized in situ by ARPES and low-energy electron diffraction (LEED). For these measurements, films were transferred under ultrahigh vacuum immediately following growth to an analysis chamber with a base pressure of 5×10^{-11} Torr equipped with a helium plasma discharge lamp, a hemispherical electron analyzer (VG Scienta R4000), and a four-grid LEED optics (SPECS ErLEED 150).

A subset of films studied by XRD and transport were also imaged using cross-sectional STEM. Cross-sectional specimens were prepared using the standard focused ion beam (FIB) lift-out process on a Thermo Scientific Helios G4 X FIB. High-angle annular dark-field STEM (HAADF-STEM) images were acquired on an aberration-corrected FEI Titan Themis at 300 keV with a probe convergence semi-angle of 21.4 mrad and inner and outer collection angles of 68 and 340 mrad.

Electronic structure calculations. Non-magnetic DFT calculations for the electronic structure of RuO₂ were performed using the Quantum ESPRESSO software

package^{50,51} with fully relativistic ultrasoft pseudopotentials for Ru and O⁵². We represented the Kohn-Sham wavefunctions in a basis set of plane waves extending up to a kinetic energy cutoff of 60 Ry, and used a cutoff of 400 Ry for representing the charge density. Brillouin zone integrations were carried out on an $8 \times 8 \times 12$ k -mesh with 70 meV of Gaussian smearing. Perdew, Burke, and Ernzerhof's parametrization of the generalized gradient approximation was employed as the exchange-correlation functional⁵³, supplemented by an on-site correction of $+U_{\text{eff}} = U - J = 2$ eV within spheres surrounding the Ru sites, following Ref. 13.

After obtaining self-consistent Kohn-Sham eigenstates via DFT, we used the pw2wannier and Wannier90 codes⁵⁴ to construct 20 Wannier functions spanning the manifold of eigenstates surrounding E_F (20 = 10 d -orbitals per Ru atom \times 2 Ru atoms per unit cell). Following Ref. 55, to account for the non-symmorphic space group symmetries of rutile crystal structures, we referenced the trial orbitals employed in the Wannierisation routine to locally rotated coordinate systems centered on the two Ru sites within each unit cell. Orbital designations employed in the main text such as $d_{||}$ and (d_{xz}, d_{yz}) refer to projections onto this basis of Wannier functions. The more computationally efficient Wannier basis was used to calculate quantities that required dense k meshes to be properly converged, such as the projected Fermi surface in Fig. 3d ($51 \times 51 \times 51$ k -mesh) and the near- E_F density of states traces in Fig. 4a ($32 \times 32 \times 48$ k -meshes).

Because the RuO₂ samples studied in this work are thin films subject to biaxial epitaxial strains imposed by differently oriented rutile TiO₂ substrates, we performed DFT + Wannier calculations of the electronic structure for several different crystal structures of RuO₂ as described in Supplementary Note 5 and Supplementary Table 1. We used the ISOTROPY software package⁵⁶ to study distortions of the parent tetragonal rutile crystal structure that are induced in biaxially strained thin films. Crystal structures and Wannier functions were visualized using the VESTA software package⁵⁷.

Electron-phonon coupling calculations. To generate the inputs required for the electron-phonon coupling calculations described below, first-principles electronic structure and phonon calculations were performed using the Quantum ESPRESSO software package with norm-conserving pseudopotentials and plane-wave basis sets^{50,51}. Here we employed a kinetic energy cutoff of 160 Ry, an electronic momentum k -point mesh of $16 \times 16 \times 24$, 20 meV of Methfessel-Paxton smearing for the occupation of the electronic states, and a tolerance of 10^{-10} eV for the total energy convergence. The generalized gradient approximation as implemented in the PBEsol functional⁵⁸ was employed as the exchange-correlation functional. For the Wannier interpolation, we used an interpolating electron-momentum mesh of $8 \times 8 \times 12$ and a phonon-momentum mesh of $2 \times 2 \times 3$. Results for bulk RuO₂ were calculated using the crystal structure that minimizes the DFT-computed total energy with the PBEsol functional: ($a = 4.464$ Å, $c = 3.093$ Å) and $x_{\text{oxygen}} = 0.3062$. Results for strained RuO₂(110) were calculated by changing the lattice constants of this simulated bulk crystal structure by +2.3% along [110], -4.7% along [001], +2.2% along [110], and setting $x_{\text{oxygen}} = y_{\text{oxygen}} = 0.2996$. The lattice parameter along [110] and internal coordinates of this simulated RuO₂(110) structure were determined by allowing the structure to relax so as to (locally) minimize the DFT-computed total energy.

Electron-phonon coupling calculations were performed using the EPW code⁵⁹, using an interpolated electron-momentum mesh of $32 \times 32 \times 48$ and an interpolated phonon-momentum mesh of $8 \times 8 \times 12$. The isotropic Eliashberg spectral function $\alpha^2F(\omega)$ and total electron-phonon coupling constant $\lambda_{\text{el-ph}}$ (integrated over all phonon modes and wavevectors) were calculated with a phonon smearing of 0.2 meV. From the calculated $\alpha^2F(\omega)$ and $\lambda_{\text{el-ph}}$, we estimated the superconducting transition temperature using the semi-empirical McMillan-Allen-Dynes formula^{60,61}:

$$T_c = \frac{\omega_{\text{log}}}{1.2} \exp \left[-\frac{1.04(1 + \lambda_{\text{el-ph}})}{\lambda_{\text{el-ph}} - \mu^*(1 + 0.62\lambda_{\text{el-ph}})} \right] \quad (2)$$

Data availability

The data supporting the findings of this study are available within the paper and supplementary information. Data connected to the study from PARADIM facilities are available at paradim.org. Any additional data connected to the study are available from the corresponding author upon reasonable request.

Received: 19 August 2020; Accepted: 19 November 2020;

Published online: 04 January 2021

References

- Carbotte, J. P. Properties of boson-exchange superconductors. *Rev. Mod. Phys.* **62**, 1027–1157 (1990).
- Morel, P. & Anderson, P. W. Calculation of the superconducting state parameters with retarded electron-phonon interaction. *Phys. Rev.* **125**, 1263–1271 (1962).
- Hamlin, J. J. Superconductivity in the metallic elements at high pressures. *Phys. C* **514**, 59–76 (2015).
- Burganov, B. et al. Strain control of fermiology and many-body interactions in two-dimensional ruthenates. *Phys. Rev. Lett.* **116**, 197003 (2016).
- Ohtomo, A. & Hwang, H. Y. A high-mobility electron gas at the LaAlO₃/SrTiO₃ heterointerface. *Nature* **427**, 423 (2004).
- Kawasaki, J. K. et al. Rutile IrO₂/TiO₂ superlattices: a hyperconnected analog to the Ruddeldsen-Popper structure. *Phys. Rev. Mater.* **2**, 054206 (2018).
- Lock, J. M. & Bragg, W. L. Penetration of magnetic fields into superconductors III. Measurements on thin films of tin, lead and indium. *Proc. R. Soc. Lond. Ser. A* **208**, 391–408 (1951).
- Locquet, J.-P. et al. Doubling the critical temperature of La_{1.9}Sr_{0.1}CuO₄ using epitaxial strain. *Nature* **394**, 453 (1998).
- Si, W., Li, H.-C. & Xi, X. X. Strain and oxygenation effects on superconductivity of La_{1.85}Sr_{0.15}CuO₄ thin films. *Appl. Phys. Lett.* **74**, 2839–2841 (1999).
- Si, W. & Xi, X. X. Epitaxial-strain-induced insulator-superconductor transition in undoped and lightly doped La₂CuO₄. *Appl. Phys. Lett.* **78**, 240–242 (2001).
- Bozovic, I., Logvenov, G., Belca, I., Narimbetov, B. & Sveklo, I. Epitaxial strain and superconductivity in La_{2-x}Sr_xCuO₄ thin films. *Phys. Rev. Lett.* **89**, 107001 (2002).
- Engelmann, J. et al. Strain induced superconductivity in the parent compound BaFe₂As₂. *Nat. Commun.* **4**, 2877 (2013).
- Berlijn, T. et al. Itinerant antiferromagnetism in RuO₂. *Phys. Rev. Lett.* **118**, 077201 (2017).
- Burdett, J. K., Hughbanks, T., Miller, G. J., Richardson, J. W. & Smith, J. V. Structural-electronic relationships in inorganic solids: powder neutron diffraction studies of the rutile and anatase polymorphs of titanium dioxide at 15 and 295 K. *J. Am. Chem. Soc.* **109**, 3639–3646 (1987).
- Lin, J. J. et al. Low temperature electrical transport properties of RuO₂ and IrO₂ single crystals. *J. Phys.: Condens. Matter* **16**, 8035 (2004).
- Ryden, W. D., Lawson, A. W. & Sartain, C. C. Electrical transport properties of IrO₂ and RuO₂. *Phys. Rev. B* **1**, 1494–1500 (1970).
- Pinto, N. et al. Dimensional crossover and incipient quantum size effects in superconducting niobium nanofilms. *Sci. Rep.* **8**, 4710 (2018).
- Meyer, T. L., Jiang, L., Park, S., Egami, T. & Lee, H. N. Strain-relaxation and critical thickness of epitaxial La_{1.85}Sr_{0.15}CuO₄ films. *APL Mater.* **3**, 126102 (2015).
- Gozar, A. et al. High-temperature interface superconductivity between metallic and insulating copper oxides. *Nature* **455**, 782–785 (2008).
- He, S. et al. Phase diagram and electronic indication of high-temperature superconductivity at 65 K in single-layer FeSe films. *Nat. Mater.* **12**, 605–610 (2013).
- Lee, J. J. et al. Interfacial mode coupling as the origin of the enhancement of T_c in FeSe films on SrTiO₃. *Nature* **515**, 245–248 (2014).
- Paik, H. et al. Transport properties of ultra-thin VO₂ films on (001) TiO₂ grown by reactive molecular-beam epitaxy. *Appl. Phys. Lett.* **107**, 163101 (2015).
- Quackenbush, N. F. et al. Reducing orbital occupancy in VO₂ suppresses Mott physics while Peierls distortions persist. *Phys. Rev. B* **96**, 081103 (2017).
- Yoshimatsu, K., Sakata, O. & Ohtomo, A. Superconductivity in Ti₄O₇ and γ -Ti₃O₅ films. *Sci. Rep.* **7**, 12544 (2017).
- Goodenough, J. B. The two components of the crystallographic transition in VO₂. *J. Solid State Chem.* **3**, 490–500 (1971).
- Eyert, V., Horny, R., Hoeck, K.-H. & Horn, S. Embedded Peierls instability and the electronic structure of MoO₂. *J. Phys.: Condens. Matter* **12**, 4923 (2000).
- Mackenzie, A. P. et al. Quantum oscillations in the layered perovskite superconductor Sr₂RuO₄. *Phys. Rev. Lett.* **76**, 3786–3789 (1996).
- Mravlje, J. et al. Coherence-incoherence crossover and the mass-renormalization puzzles in Sr₂RuO₄. *Phys. Rev. Lett.* **106**, 096401 (2011).
- Tamai, A. et al. High-resolution photoemission on Sr₂RuO₄ reveals correlation-enhanced effective spin-orbit coupling and dominantly local self-energies. *Phys. Rev. X* **9**, 021048 (2019).
- Ricco, S. et al. In situ strain tuning of the metal-insulator-transition of Ca₂RuO₄ in angle-resolved photoemission experiments. *Nat. Commun.* **9**, 4535 (2018).
- Sutter, D. et al. Orbital selective breakdown of Fermi liquid quasiparticles in Ca_{1.8}Sr_{0.2}RuO₄. *Phys. Rev. B* **99**, 121115 (2019).
- Sutter, D. et al. Hallmarks of Hund's coupling in the Mott insulator Ca₂RuO₄. *Nat. Commun.* **8**, 15176 (2017).
- Jovic, V. et al. Dirac nodal lines and flat-band surface state in the functional oxide RuO₂. *Phys. Rev. B* **98**, 241101 (2018).
- Passenheim, B. C. & McCollum, D. C. Heat capacity of RuO₂ and IrO₂ between 0.54 and 10 K. *J. Chem. Phys.* **51**, 320–321 (1969).
- Glassford, K. M. & Chelikowsky, J. R. Electron transport properties in RuO₂ rutile. *Phys. Rev. B* **49**, 7107–7114 (1994).

36. Marcus, S. M. & Butler, S. R. Measurement of the de Haas-van Alphen effect in the rutile structure RuO₂. *Phys. Lett. A* **26**, 518–519 (1968).
37. Slivka, R. T. & Langenberg, D. N. Azbel-Kaner cyclotron resonance in ruthenium dioxide. *Phys. Lett. A* **28**, 169–170 (1968).
38. Graebner, J. E., Greiner, E. S. & Ryden, W. D. Magnetothermal oscillations in RuO₂, OsO₂, and IrO₂. *Phys. Rev. B* **13**, 2426–2432 (1976).
39. Smith, T. F. & Chu, C. W. Will pressure destroy superconductivity? *Phys. Rev.* **159**, 353–358 (1967).
40. Hopfield, J. J. Angular momentum and transition-metal superconductivity. *Phys. Rev.* **186**, 443–451 (1969).
41. Ishizuka, M., Iketani, M. & Endo, S. Pressure effect on superconductivity of vanadium at megabar pressures. *Phys. Rev. B* **61**, R3823–R3825 (2000).
42. Steppke, A. et al. Strong peak in T_c of Sr₂RuO₄ under uniaxial pressure. *Science* **355**, eaaf9398 (2017).
43. Muraoka, Y. & Hiroi, Z. Metal-insulator transition of VO₂ thin films grown on TiO₂ (001) and (110) substrates. *Appl. Phys. Lett.* **80**, 583–585 (2002).
44. Aetukuri, N. B. et al. Control of the metal-insulator transition in vanadium dioxide by modifying orbital occupancy. *Nat. Phys.* **9**, 661–666 (2013).
45. Alves, L. M. S. et al. Unconventional metallic behavior and superconductivity in the K-Mo-O system. *Phys. Rev. B* **81**, 174532 (2010).
46. Alves, L. M. S. et al. Superconductivity and magnetism in the K_xMoO_{2-δ}. *J. Appl. Phys.* **112**, 073923 (2012).
47. Parker, D., Idrobo, J. C., Cantoni, C. & Sefat, A. S. Evidence for superconductivity at $T_c = 12$ K in oxygen-deficient MoO_{2-δ} and properties of molybdenum arsenide and oxide binaries. *Phys. Rev. B* **90**, 054505 (2014).
48. Yamamoto, Y., Nakajima, K., Ohsawa, T., Matsumoto, Y. & Koinuma, H. Preparation of atomically smooth TiO₂ single crystal surfaces and their photochemical property. *Jpn. J. Appl. Phys.* **44**, L511 (2005).
49. He, Y., Langsdorf, D., Li, L. & Over, H. Versatile model system for studying processes ranging from heterogeneous to photocatalysis: epitaxial RuO₂(110) on TiO₂(110). *J. Phys. Chem. C* **119**, 2692–2702 (2015).
50. Giannozzi, P. et al. QUANTUM ESPRESSO: a modular and open-source software project for quantum simulations of materials. *J. Phys.: Condens. Matter* **21**, 395502 (2009).
51. Giannozzi, P. et al. Advanced capabilities for materials modelling with Quantum ESPRESSO. *J. Phys.: Condens. Matter* **29**, 465901 (2017).
52. Dal Corso, A. Pseudopotentials periodic table: from H to Pu. *Comp. Mater. Sci.* **95**, 337–350 (2014).
53. Perdew, J. P., Burke, K. & Ernzerhof, M. Generalized gradient approximation made simple. *Phys. Rev. Lett.* **77**, 3865–3868 (1996).
54. Mostofi, A. A. et al. An updated version of wannier90: a tool for obtaining maximally-localised Wannier functions. *Comput. Phys. Commun.* **185**, 2309–2310 (2014).
55. Eyert, V. The metal-insulator transitions of VO₂: a band theoretical approach. *Ann. der Phys.* **11**, 650–704 (2002).
56. Stokes, H. T., Hatch, D. M. & Campbell, B. J. ISOTROPY Software Suite. [iso.byu.edu](http://www.byu.edu).
57. Momma, K. & Izumi, F. VESTA 3 for three-dimensional visualization of crystal, volumetric and morphology data. *J. Appl. Crystallogr.* **44**, 1272–1276 (2011).
58. Perdew, J. P. et al. Restoring the density-gradient expansion for exchange in solids and surfaces. *Phys. Rev. Lett.* **100**, 136406 (2008).
59. Ponce, S., Margine, E. R., Verdi, C. & Giustino, F. EPW: electron-phonon coupling, transport and superconducting properties using maximally localized Wannier functions. *Comput. Phys. Commun.* **209**, 116–133 (2016).
60. McMillan, W. L. Transition temperature of strong-coupled superconductors. *Phys. Rev.* **167**, 331–344 (1968).
61. Allen, P. B. & Dynes, R. C. Transition temperature of strong-coupled superconductors reanalyzed. *Phys. Rev. B* **12**, 905–922 (1975).

Acknowledgements

The authors thank Y. Li for assistance with electrical transport measurements. This work was supported through the National Science Foundation (Platform for the Accelerated Realization, Analysis, and Discovery of Interface Materials, PARADIM) under Cooperative Agreement No. DMR-1539918, NSF DMR-1709255, the Air Force Office of Scientific Research Grant No. FA9550-15-1-0474, and the Department of Energy (Award No. DE-SC0019414). This research was funded in part by the Gordon and Betty Moore Foundation's EPiQS Initiative through Grant Nos. GBMF3850 and GBMF9073 to Cornell University. This work made use of the Cornell Center for Materials Research (CCMR) Shared Facilities, which are supported through the NSF MRSEC Program (No. DMR-1719875). The FEI Titan Themis 300 was acquired through NSF-MRI-1429155, with additional support from Cornell University, the Weill Institute, and the Kavli Institute at Cornell. Device fabrication and substrate preparation were performed in part at the Cornell NanoScale Facility, a member of the National Nanotechnology Coordinated Infrastructure (NNCI), which is supported by the NSF (Grant No. ECCS-1542081).

Author contributions

H.P., N.J.S., and H.P.N. synthesized the samples by MBE. J.P.R., H.P., N.J.S., and H.P.N. characterized the samples by XRD. J.P.R., L.M., and Y.L. characterized the samples by electrical transport; L.M. lithographically patterned resistivity bridges on select films. J.P.R., J.K.K., J.N.N., and B.D.F. characterized the samples by ARPES and LEED. B.H.G. characterized the samples by STEM, J.P.R. performed DFT calculations of the electronic structure, and B.P. performed DFT-based calculations of the electron-phonon coupling. L.F.K., D.G.S., and K.M.S. supervised the various aspects of this project. J.P.R. and K.M.S. wrote the manuscript with input from all authors.

Competing interests

The authors declare no competing interests.

Additional information

Supplementary information is available for this paper at <https://doi.org/10.1038/s41467-020-20252-7>.

Correspondence and requests for materials should be addressed to J.P.R. or K.M.S.

Peer review information *Nature Communications* thanks the anonymous reviewers for their contribution to the peer review of this work.

Reprints and permission information is available at <http://www.nature.com/reprints>

Publisher's note Springer Nature remains neutral with regard to jurisdictional claims in published maps and institutional affiliations.



Open Access This article is licensed under a Creative Commons Attribution 4.0 International License, which permits use, sharing, adaptation, distribution and reproduction in any medium or format, as long as you give appropriate credit to the original author(s) and the source, provide a link to the Creative Commons license, and indicate if changes were made. The images or other third party material in this article are included in the article's Creative Commons license, unless indicated otherwise in a credit line to the material. If material is not included in the article's Creative Commons license and your intended use is not permitted by statutory regulation or exceeds the permitted use, you will need to obtain permission directly from the copyright holder. To view a copy of this license, visit <http://creativecommons.org/licenses/by/4.0/>.

© The Author(s) 2021